Plasma Chemistry and Plasma Processing, Vol. 2, No. 3, 1982

Influence of Velocity and Surface Temperature of Alumina Particles on the Properties of Plasma Sprayed Coatings

A. Vardelle,[1] M. Vardelle,[1] and P. Fauchais[1]

Received April 6, 1982; revised June 24, 1982

In this paper are described the main characteristics of the plasma spraying process of alumina deposits, i.e., the temperature and flow field of the plasma jets obtained with the classical spraying torches, the injection of the particles into the plasma jet, the particle surface temperature and velocities in the plasma (measured for calibrated alumina particles), and the coating generation. The measurements on the alumina particles are compared with the predictions of a mathematical model. The experimental and computed particle velocities are in rather good agreement. However, this is not the case for the particle surface temperature. Possible reasons for the discrepancy are proposed (influence of the carrier gas, thermophoretic forces, and poor penetration of the particles into the plasma core even for an injection velocity twice that of the optimal calculated one, as shown by recent measurements). Finally the correlations between the particle velocities and surface temperature, and the properties of the alumina coating (porosity, crystal structure, mechanical properties) are studied.

KEY WORDS: Plasma spraying process; particle temperature and velocities; plasma diagnostics; alumina coatings.

1. INTRODUCTION

The formation of protective coatings from a stream of molten metal or ceramic particles was first developed using combustion flames into which the spray material was fed as powder, wire, or rod. In the 1960's commercial plasma spraying equipment became available in which a D.C. plasma jet was used to melt a powder feed and project the droplets at high velocity against the material to be coated. The major advantage over the flame spraying process is the higher particle velocity obtainable (up to 500 m/s), and the high temperatures achieved in the plasma jet (up to 15,000 K) also make it possible to melt even the most refractory materials to produce

[1] Equipe Céramiques L.A. 320, Université de Limoges, France.

0272-4324/82/0900-0255$03.00/0

high-quality coatings. Plasma spraying is therefore particularly suitable for the formation of ceramic coatings for wear, thermal, and corrosion protection.

Plasma spraying[1] differs considerably from other surface treatments by its specific characteristics, viz.:

The energy source is separated from the substrate: for this reason plasma spraying may be a cold substrate process.
The particles interact in some way chemically and physically with the environment during the flight.
The sprayed layer is built up particle by particle.
The particles are cooled very fast after arriving at the substrate (splat cooling).
The sprayed layer shows a structure of lamellae.
Thermal spraying makes it possible to produce coatings of essentially different materials.

As usual, the scientific research lags behind the technical application, and plasma spraying has developed, to a large extent, by empirical means with relatively little scientific understanding of the mechanisms involved in coating formation and of the factors controlling the structure and properties of the coating. This is because the range of temperatures and the time scale of the various events are generally outside the usual experimental conditions encountered in materials processing and sophisticated techniques must be used to make significant progress. However, a better understanding of plasma spraying is now emerging, as shown by recent reviews.[1–4]

To achieve the best spraying conditions of plasma-sprayed deposits with the required macroscopic properties, one has to solve many problems. First, one has to search after the physics governing the processes; second, one has to formulate the requirements for a reliable and predictable production; and third, one has to determine the limits of the field of application. But this is easier to say than to do with more than 35 main macroscopic parameters (see Table I).

Since 1975, with the development of new measuring techniques such as laser doppler anemometry or in-flight pyrometry (see the Appendix) and with the automation of the spectroscopic measurements, it is, however, possible to follow statistically what happens to the particles in flight into the plasma jet and especially to attempt to correlate the physical properties of the plasma-sprayed deposits with the surface temperature and velocity of the particles upon impact.

That is why, starting from alumina for which the physical and chemical properties as functions of the temperature are well known, we will describe:

Table I. Main Parameters of Plasma Spraying Process

Power and energy	Spraying material	Substrate	Powder feeder	Spraying conditions
Voltage Current intensity Nature of the plasma gas Flow rate of the gas Nature and design of the electrodes of the plasma torch	Size of the powder particles Particle shape Particle diameter Particle size distribution Physical and chemical properties of the powder (melting point, thermal conductivity, etc.)	Physical and chemical properties of the substrate (thermal linear expansion coefficient, etc.) Surface roughness, oxidation and cleanliness of the substrate Substrate temperature during spraying process	Nature and mass flow rate of the carrier gas of the particles Powder mass flow rate Location and inclination of the powder injector Number of powder injectors Powder injection velocity	Distance between the nozzle exit and the substrate Relative movement between the substrate and the torch Ambient atmosphere or controlled atmosphere Method cooling of the substrate

the main characteristics of the plasma jets obtained with the classical spraying torches (Section 2.2),
the difficulties in injecting the particles into the plasma jet (Section 2.3),
the temperatures and velocities of the particles in flight into the plasma (Section 2.3),
the coating generation (Section 3.1),
the correlations existing between the particle velocities and surface temperatures and the properties of the sprayed deposit: porosity, crystal structure, and mechanical properties (Section 3.2).

2. SPRAYING DEVICE CHARACTERISTICS

2.1. Plasma Torches

The plasma torches used in spraying at atmospheric pressure have usually a maximum power of 90 kW and are based on a concept first given by Gage.[5] A direct current (D.C.) arc is struck between a cathode rod (usually made of thoriated tungsten) and a copper nozzle used as anode (the cathode rod is along the axis of the nozzle.[6,7] Stabilization of the arc is of cold wall type, and the gas injection is either tangential or longitudinal, forcing the arc to strike into the nozzle which is intensively water cooled. For this study we have used a 30-kW D.C. plasma generator made in our laboratory,[8] but numerous torches of this type are commercially available, for example, in the United States from Plasmadyne, Metco, and Avco, in Belgium from Arcos, in France from Air Liquide, in Poland from the Institute of Swierk, and in Switzerland from Plasmatechnic.

2.2. Characteristics of the Corresponding Plasma Jets

The characteristics (temperature and velocity distributions) of the plasmas jets are functions of the pressure, of the gases used (nature, flow rates, injection mode), of the dimensions and the shape of the electrodes, of the electrical power, of the current intensity, etc.

To determine the characteristics of such plasma jets we use the following techniques[9] (see Appendix).

a. To measure the temperature of the plasma jet we use, for $T > 6000$ K, spectroscopic methods (absolute line intensity of N I or Ar I) automated with a data acquisition system controlled by a computer performing the Abel's inversion,[10] and for $T < 4000$ K we use thermocouples or the melting points of different materials (correcting, of course, the measurements for the radiative and conductive losses). Such methods make it

possible to determine the temperature (under local thermal equilibrium, L.T.E.) either in the hot zone of the jet or in the plume.

b. To measure the velocity of the plasma jet we use laser anemometry (two-point method) with small alumina particles (less than 3 μm diameter) injected directly with the plasma gas into the arc chamber. However, due to the high luminosity of the plasma just after the nozzle exit, the measurements could be performed only 2 cm downstream from the nozzle exit. One has to emphasize that such methods are local methods involving small volumes: $10 \times 100 \times 100$ μm for the plasma velocity.

The plasma gases used in spraying are either argon or nitrogen, in both cases with hydrogen added in order to improve the heat transfer.[11] This is due to the fact that, as soon as the plasma temperature is greater than 4500 K (i.e., the dissociation temperature of H_2), the mean integrated thermal conductivity is about 5 W/m/K for H_2 compared to 0.1 for N_2 and 0.04 for Ar. That is why we have used mixtures of Ar–H_2 or N_2–H_2 for our experiments.

First we have tried to determine for these three gases the variations of the temperatures and velocities with the nature of the gas and the flow rate and with the diameter and length of the nozzle. Of course, due to the high radial gradients (up to 4000 K/mm and 200 m/s/mm), the comparisons we are going to summarize are relative to the temperatures and velocities on the plasma jet axis just at the nozzle exit.

2.2.1. Plasma Velocity

Due to the viscosities of the gases (Ar, N_2, H_2) at high temperature, one gets, for the same pressure, the same shape and dimensions of the electrodes, the same current intensity (meaning a very different power; for example, with 200 A and a 5-mm-diameter nozzle, the voltage is 20 V with argon, 60 V with nitrogen, and 120 V with hydrogen at atmospheric pressure) the highest velocity, 1200 m/s, with pure hydrogen, and then successively 800 m/s with nitrogen and 400 m/s with argon.

2.2.2. Plasma Temperature

Under the same conditions (200 A, 5-mm-nozzle diameter) the measured temperatures of the plasma jet, within 1000 K, are equivalent for argon, nitrogen, and hydrogen (about the same ionization potential).

2.2.3. Influence of Nozzle Dimensions

Under the same conditions of current intensity and nature and mass flow rate of the gas, an increase of the nozzle diameter usually lowers the

temperature a little (between 3 and 10% for an increase of 1 mm of the diameter after our measurements) and reduces more markedly the velocities, but the plasma jet is less convergent and the radial component of the velocity increases from 5 to 10% of the axial one when the nozzle diameter increases from 6 to 8 mm.

The length of the nozzle has to be adjusted carefully to the nozzle diameter and the nature and mass flow rate of the gas. If it is too short, the arc strikes outside of the nozzle and the jet flow is perturbed; if the nozzle is too long, the cooling has to be increased and the thermal yield of the plasma generator is lowered.

2.2.4. Choice of the Plasma Parameters

Our purpose was to perform the measurements under the usual industrial spraying conditions. That is why we have chosen[12] a mixture of argon and hydrogen (75 Nl/min of argon and 37 Nl/min of hydrogen) with a nozzle diameter of 8 mm and a length of the cylindrical nozzle of 22 mm (see Fig. 1a).

In order to compare the same things and to demonstrate the possibility of using a cheaper mixture, N_2/H_2, we have adjusted the nozzle diameter and mass flow rate to obtain the same power level, i.e., a nozzle of 6 mm

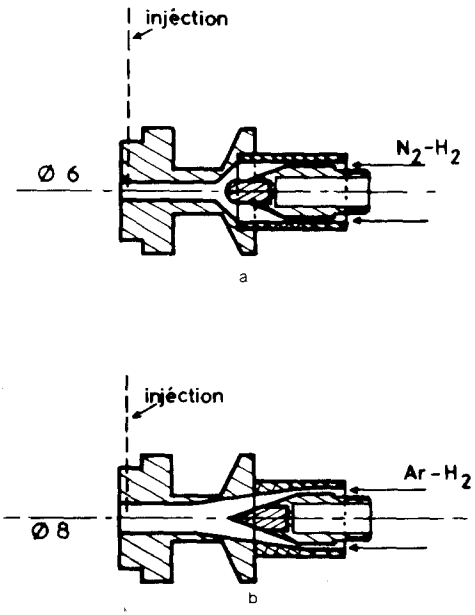

Fig. 1. Schematic of the nozzle dimensions for (a) $Ar–H_2$ and (b) $N_2–H_2$ plasmas.

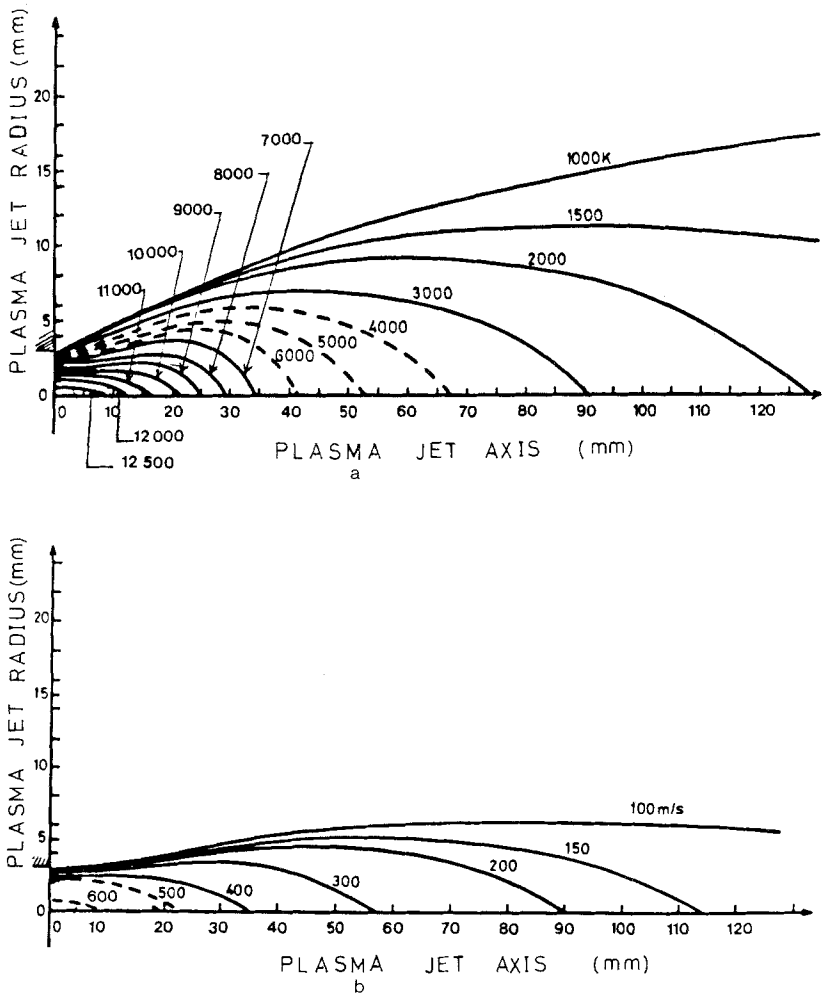

Fig. 2. Temperature (a) and axial velocity (b) isocontours of a nitrogen–hydrogen D.C. plasma jet at $P = 29$ kW, $D_{N_2} = 37$ Nl/min, $D_{H_2} = 27$ Nl/min.

diameter and 26 mm length with a flow rate of 37 Nl/min of nitrogen and of 27 Nl/min of hydrogen (see Fig. 1b). Typical results obtained with the N_2/H_2 plasma at a power level of 29 kW are given in Fig. 2a and b. Figure 2a gives the temperature isocontours. We note that the plasma jet can be divided into three regions: the core region in which the plasma temperature is relatively constant, 12,000–12,500 K, extending to about 10 to 12 mm from the torch nozzle. This is followed by a transition region in which the

plasma temperature falls rapidly to less than 3000 K at 100 mm from the nozzle exit. In the last region, the gas temperature drops gradually as the gas is mixed with the entrained ambient air. The radial temperature profiles are particularly steep over the core region. The presence of such steep temperature gradients explains the problem of the thermal treatment of the particles in a D.C. plasma jet, which requires very close control of the particle injection conditions into the plasma.

In Fig. 2b the axial velocity isocontours are shown. As mentioned before, these were obtained by studying with laser anemometry (two-points method; see the Appendix) the flow seeded by small particles that are assumed to follow the flow field. It is, however, particularly difficult to ensure the uniform distribution of the seeding particles and their penetration into the core region, so it was not possible to obtain significant gas velocity in this region (approximately the first two centimeters downstream the nozzle exit). Beyond the core region, the plasma velocity drops rapidly with increase in distance from the torch nozzle.

Similar results at the same power level of 29 kW are represented in Fig. 3a and b for an Ar/H_2 mixture. It can be seen (Fig. 3a) that the diameter of this jet is greater than the one of N_2/H_2 (this is probably due to the increase of the nozzle diameter) and that the core and plume of the jet are also longer (for the core, about 30 mm for N_2/H_2 and 50 mm for Ar/H_2 on the axis). The velocities in the N_2/H_2 jet are higher than the ones in the Ar/H_2 jet, a phenomenon due probably to the smaller viscosity of the N_2/H_2 mixture and to the smallest nozzle diameter with N_2/H_2.

2.3. Particle Injection, Trajectories, Velocities, and Surface Temperature

The material to be sprayed is introduced as small particles (diameters between 3 and 70 μm) into the plasma jet, accelerated to velocities greater than 100 m/s, and melted (as expected).

The powders are injected orthogonally to the plasma jet 2 mm before the end of the cylindrical pipe of the nozzle. In order to understand exactly what happens to the particles, we have used monocrystalline alumina consisting of α-Al_2O_3 (purity 99.99%) with narrow particle sizes: 9 ± 2 μm, 18.5 ± 3 μm, and 46 μm ± 4 μm (see, for example, Fig. 3 in ref. 12). These powders were provided by the Nuclear Center of Saclay (DGI).

2.3.1. Model

Before proceeding to the measurements of the particle velocities and temperature in flight, we have developed a two-dimensional model of

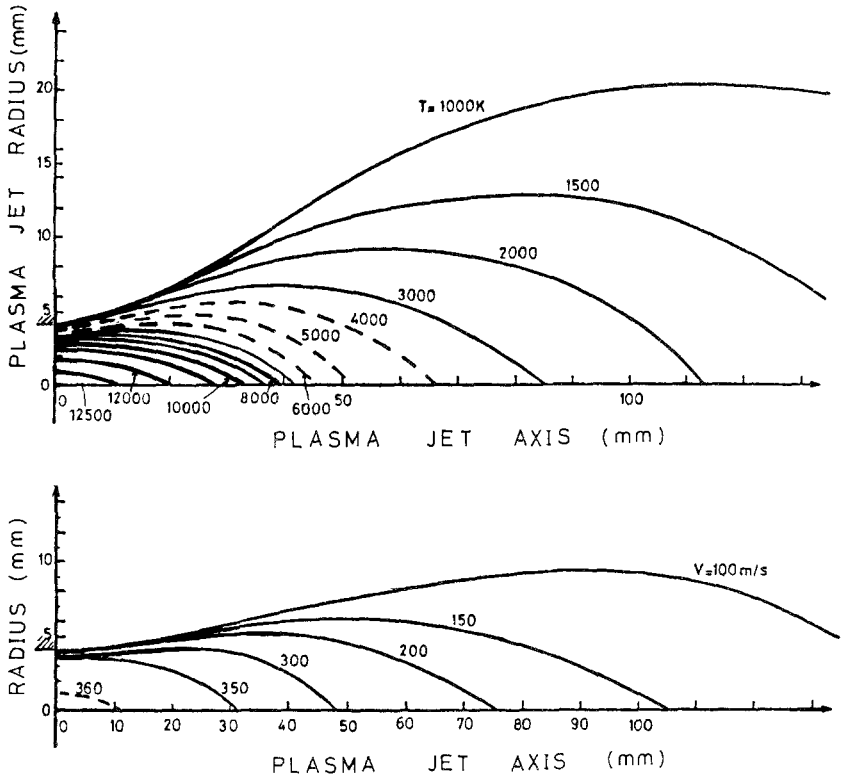

Fig. 3. Temperature (a) and axial velocity (b) isocontours of an argon–hydrogen D.C. plasma jet at $P = 29$ kW, $D_{Ar} = 75$ Nl/min, $D_{H_2} = 37$ Nl/min.

momentum and heat transfer between a solid particle and the plasma jet, including heat and phase-change propagation into the particle. For this model, which allows us to calculate the trajectories and temperature histories of the particles in the plasma jet, we have used the gas temperature and velocity profiles measured as mentioned before (see Figs. 1 and 2), and we have adopted the following assumptions: (A1) The particles are spherical. (A2) The thermal boundary layer is in thermodynamic equilibrium. (A3) The only heat transfer mechanism is gas conduction. Then the value of the Nusselt number is 2 (as demonstrated by Bourdin[11] when one uses the mean integrated thermal conductivity to take into account the steep variations of the temperature in the boundary layer around the particle:

$$\overline{k_g} = \frac{1}{T_g - T_p} \int_{T_p}^{T_g} k_g(T)\, dT \tag{1}$$

where k_g is the gas thermal conductivity, T_g is the plasma temperature far from the particle, and T_p is the particle surface temperature. The values of $\overline{k_g}$ have been calculated using a method developed by Gorse[13] in the laboratory with the composition of the plasma computed using a program developed by Bourdin.[14] (A4) The influence of the carrier gas is neglected. (A5) The temperature and velocity contours measured without carrier gas and powder feed are valid. (A7) Plasma radiation is neglected. (A8) Radiation heat losses of the particles are small compared to the heat gained from the gas: Bourdin[11] has demonstrated that this is true as soon as the plasma temperature is greater than 4000 K. (A9) The particle's thermal properties (thermal conductivity k_p and heat capacity c_p) are not temperature dependent. This simplification of the calculations is justified since during the heating phase of the particles the values obtained with a variation of 50% of k_p and c_p, which corresponds to the range encountered between room temperature and melting point, differ from the calculated surface temperature by less than 4%. As the mixtures considered have a high content of hydrogen, the ratio $\bar{k}_g/k_p$ is greater than 0.03 and the heat propagation into the alumina particles has to be taken into account.[11] The governing equations of the models have been described elsewhere,[15,16] and in such equations the thermophoresis forces have been neglected. In this first model we stop our calculations when evaporation starts.

In the absence of surface vaporization and as long as integral average properties are used to account for the steep temperature gradients in the boundary layer, the trajectories calculated with the momentum transfer equation are independent of the surface temperature of the particle. This result allows considerable computing simplification since the trajectories are determined independently as a function of the particle radius and injection velocity; then, using the gas temperature chart, it is possible to deduce a "time vs. temperature history" of the particle knowing its calculated trajectory and velocity. Otherwise stated, we determine the gas temperature "seen" by the particle during its dwell time in the jet. Using this time vs. temperature profile, the temperature repartition in the particle is determined by solving the heat equation as proposed by Murray[17] and applied to spherical particles by Yoshida.[16] The computer algorithm has been significantly improved using an iterative procedure suggested by Jamet.[18]

Such calculations have been performed for the different particle sizes under consideration. Depending upon their sizes, the particle injection velocity has a significant influence on the particle trajectories and, consequently, thermal treatment in the plasma gas: if the particle injection velocity is too low, the particles do not penetrate into the plasma jet, while if it is too fast, they cross the jet and travel to the colder zones of the

plasma. Figure 4a shows, as an example, the trajectories and velocities (relative to the plasma jet axis) of 23-μm Al_2O_3 particles in the N_2/H_2 plasma for different injection velocities, and Fig. 4b gives the corresponding plasma temperatures seen by the particles. That is why we have determined for each size the optimum injection velocity to get an axial trajectory (see Table II).

In calculating the evolution of the surface and center temperatures of a particle of 23 μm diameter, we see that it takes about 0.1 ms for its surface to reach the evaporation temperature, the temperature at which

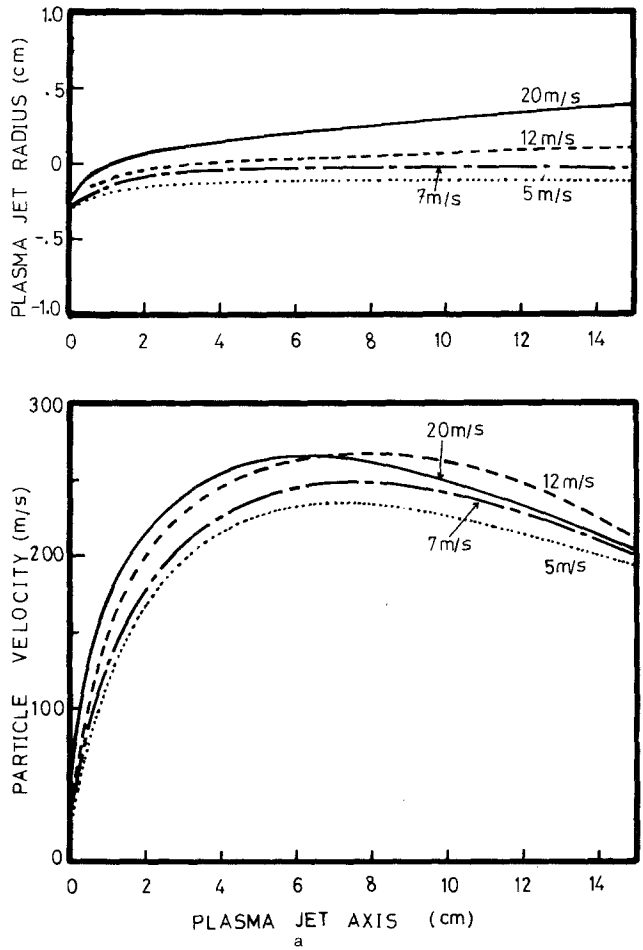

Fig. 4. (a) Trajectories of a 23-μm alumina particle for different injection velocities. N_2/H_2 plasma gas; $P = 29$ kW, $D_{N_2} = 37$ Nl/min, $D_{H_2} = 27$ Nl/min.

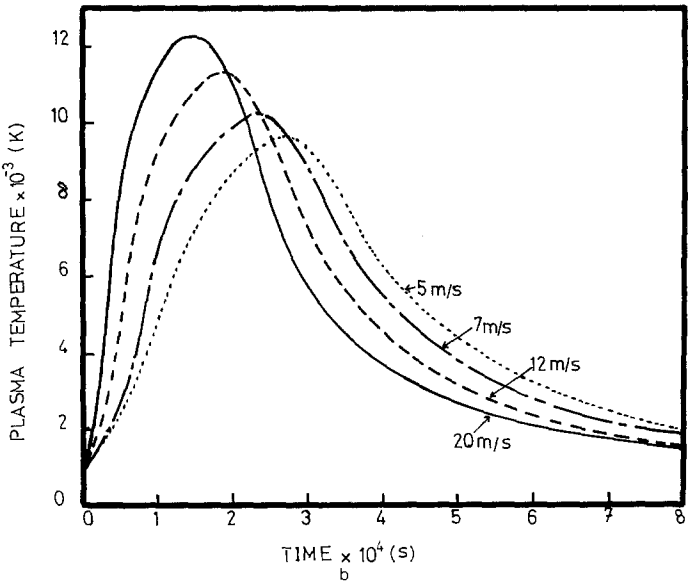

Fig. 4. (b) Plasma temperature "seen" by the particle for its different trajectories.

our model is no longer valid. That is why we have performed these heat-transfer calculations for particles of diameter greater than 80 μm for which the surface temperature never reaches the evaporation temperature. For example, Fig. 5 shows the evolution of the surface (C1) and center (C3) temperatures of a 100-μm alumina particle in the N_2/H_2 plasma together with the plasma temperature "seen" by this particle (C4). It is important to note the heat transfer phenomena: the center temperature is far below the surface temperature and reaches the melting temperature only when the surface temperature has begun to decrease; as a consequence of the heat flux continuity at the surface of the particle, the surface

Table II. N_2–H_2 Plasma Gas

Particle diameter (μm)	Optimum injection velocity	
	Experimental	Calculated
18	25	15
23	22	12
39	18	7
46	14	5

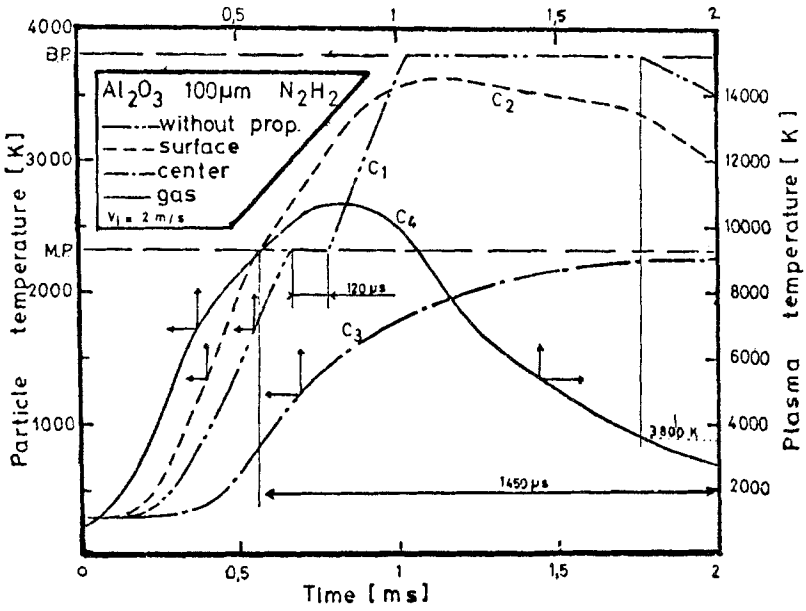

Fig. 5. Calculated particle temperature of a particle in flight into the N_2–H_2 plasma jet as a function of time. Surface temperature C2, center temperature C3, plasma temperature seen by the particle C4 ($P = 29$ kW; $D_{N_2} = 37$ Nl/min; $D_{H_2} = 27$ Nl/min).

temperature decreases with plasma gas temperature and then the inner part of the particle is heated by the outer part.

However, if the heat propagation into the particle is not taken into account, the bulk temperature of the particle (C1) is considerably higher, reaching even the boiling temperature, the plasma heat flux being entirely converted into latent heat of fusion or boiling.

2.3.2. Experimental Results

As we have already said, due to the importance of the radiative emission of the plasma itself in the flow 2 cm after the nozzle exit, the velocity measurements have been performed only 2 cm downstream of the nozzle exit, and the surface temperatures, 3 cm downstream. Thus it was not possible to compare our calculations in a straightforward manner with the measurements.

a. Trajectories and Velocities. The experiments have confirmed the necessity of an optimum injection velocity for obtaining an axial trajectory. In our experiments we have adjusted the carrier gas pressure to modify

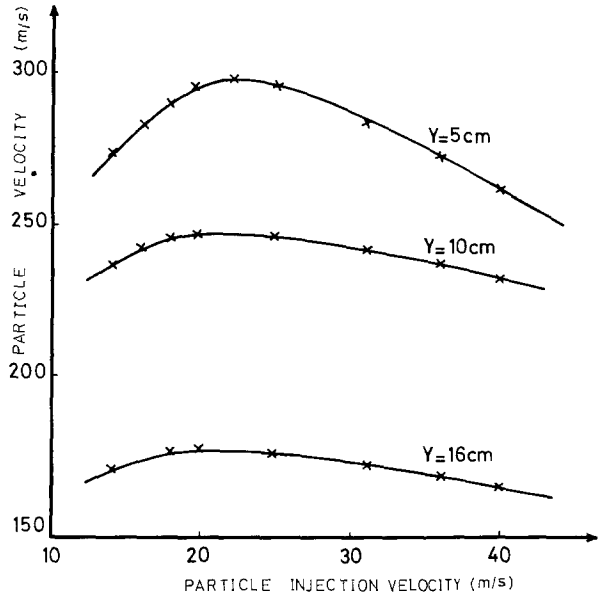

Fig. 6. Experimental velocity of alumina particles (18 μm diameter) versus injection velocity in a nitrogen–hydrogen plasma at 29 kW. The different curves correspond to velocities measured at different distances from the nozzle exit.

the injection velocity, controlled by LDA, at the exit of the powder injector. Figure 6 shows the influence of the injection velocity on the axial velocity measured at different distances from the nozzle exit (the measurements have been performed for 18 ± 2 μm alumina particles in the N_2–H_2 29-kW plasma already described; see Fig. 2). It is clear that the optimum injection velocity is 25 m/s. The optimum injection velocities have been determined for all the particles under consideration: 25 m/s for 18 μm, 22 m/s for 23 μm, 18 m/s for 39 μm, and 14 m/s for 46-μm particles. It is clear that the model (see Section 2.3.1 and Fig. 4b: maximum axial velocity of the particle for an injection velocity of 12 m/s) explains the influence of the injection velocity. However, a given axial trajectory is theoretically obtained with a lower injection velocity than the experimental one (see Table II and Fig. 4a, where the axial trajectory is obtained for 12 m/s with 23-μm particles against 22 m/s experimentally), and we will try, through our particle flux measurements, to explain such a discrepancy.

In the first part of the trajectory, the plasma gas velocity (200–600 m/s) is very high compared to the particle velocity (about 20 m/s); thus the friction force of the fluid on the particle, proportional to the relative velocity

difference, is very high and the acceleration of the particle is considerable (up to $100{,}000 \times g$). This force vanishes at the point of the trajectory where, due to the slowing of the gas, the velocities of the gas and of the particle become equal; beyond this point it becomes a breaking force. The smaller the diameter of the particle, the closer the velocities of the gas and of the particle (under 3 μm the particles may be assumed to follow the gas velocity). This is shown in Fig. 7, which represents the experimental velocity

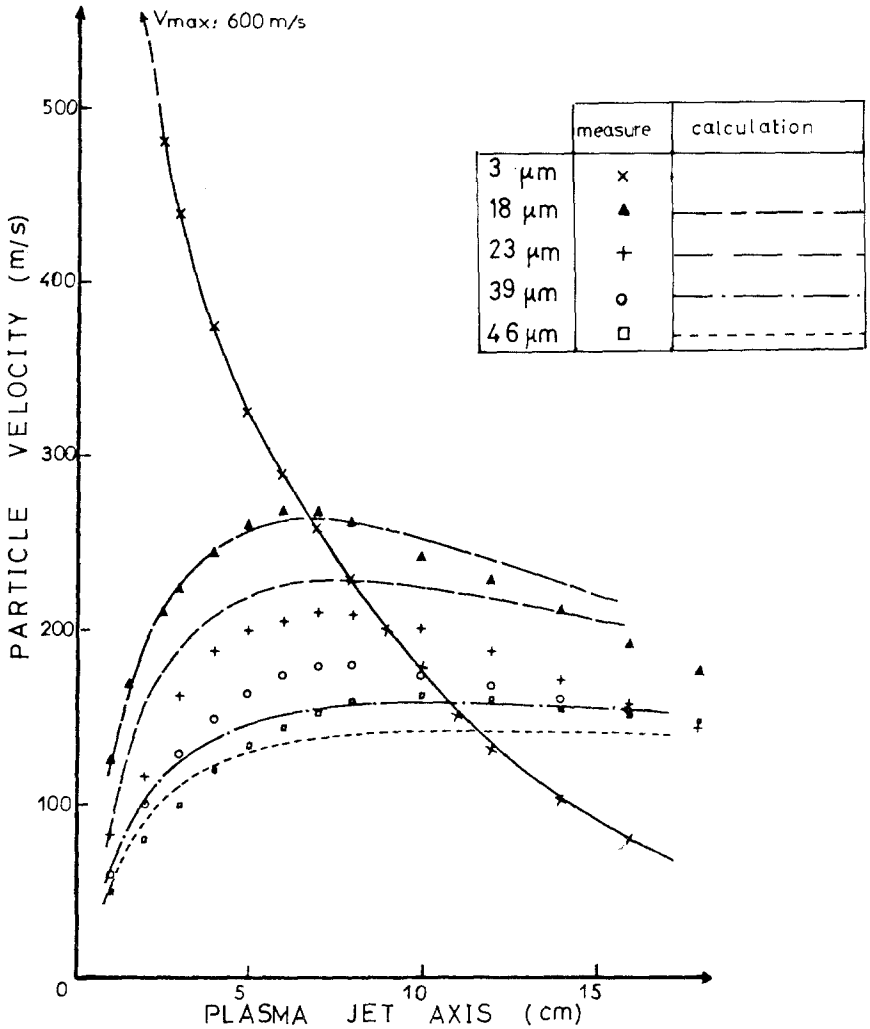

Fig. 7. Experimental velocity of alumina particles along the plasma jet axis (N_2–H_2 plasma at 29 kW) for alumina particles of different diameters.

variation along the plasma jet axis of alumina particles of different diameters (N_2/H_2 plasma jet of 29 kW). For example, the 18-μm particles reach a maximum velocity of 275 m/s 60 mm after the nozzle exit, their acceleration is about $70{,}000 \times g$, and their deceleration of the order of $20{,}000 \times g$. The biggest particles, of course, have the lowest velocities and the smallest accelerations. Similar results have been obtained with the Ar–H_2 plasma (see Fig. 14 of ref. 19) with lower velocities of about 20 to 50 m/s depending on sizes (the greatest differences exist with the smallest particles).

Figure 8 shows the measured axial and radial distribution of the axial component of the velocity of 18-μm alumina particles. This illustrates the wide range of mean velocities within the spray stream, indicating that the highest velocities are achieved along the jet axis; 60 mm after the nozzle exit, the axial velocity is 275 m/s, and 11 mm away from the axis in an orthogonal plane it is 200 m/s. Of course this distribution has been obtained using the optimum injection velocity of 25 m/s. Compared to the axial component of the velocity, the radial component is very low, as can be seen in Fig. 9. Such a radial component corresponds to an angle of divergence from an axial trajectory of less than 2° at a distance 10 cm downstream of the nozzle exit. Similar results are obtained with Ar–H_2 but with a slightly greater component of the radial velocity, probably due to the increase of the nozzle diameter.

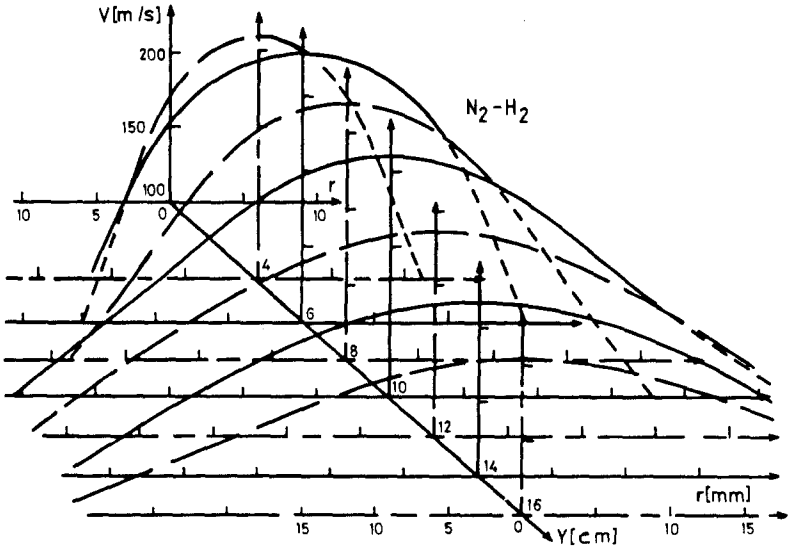

Fig. 8. Spatial distribution of the experimental velocity of alumina particles (18 ± 2 μm) in the N_2–H_2 29-kW D.C. plasma jet.

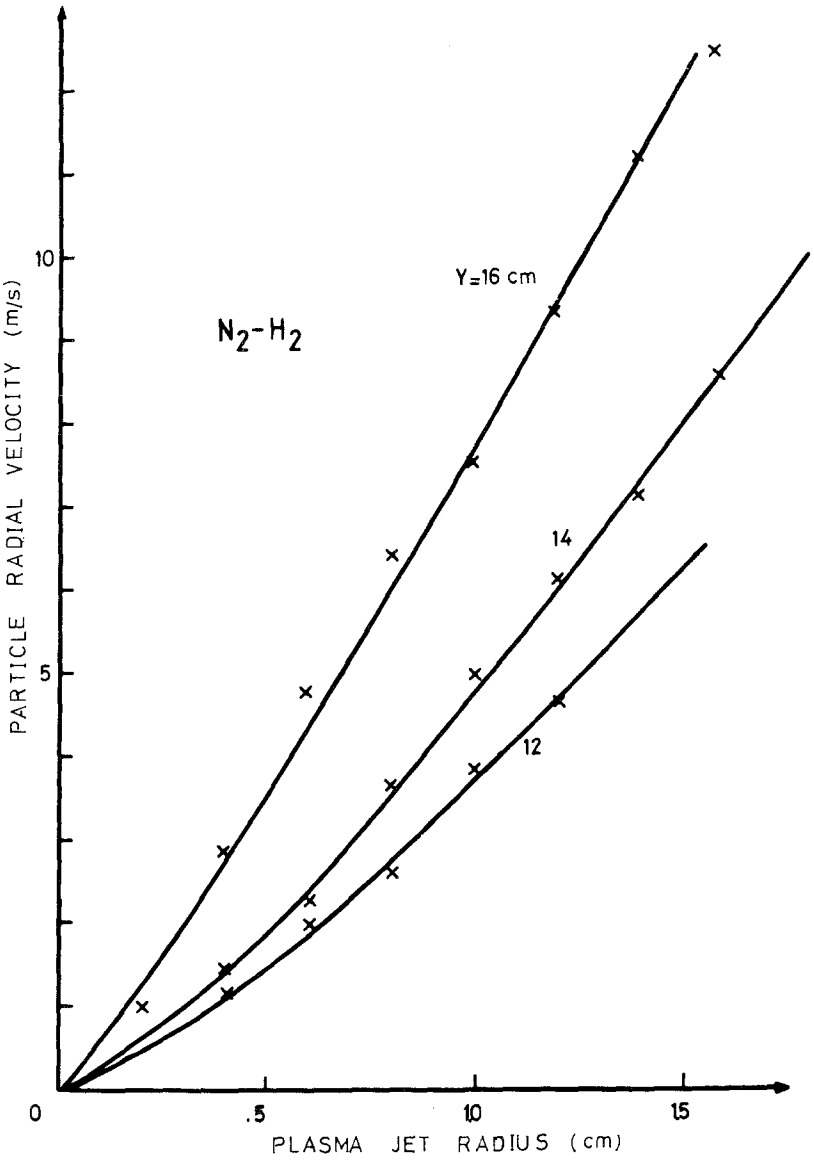

Fig. 9. Evolution of the experimental radial component of the velocity of alumina particles ($18 \pm 2\ \mu$m) versus radius in the plasma jet (plasma: N_2/H_2; $P = 29$ kW; $D_{N_2} = 37$ Nl/min; $D_{H_2} = 27$ Nl/min).

As it was impossible to perform measurements either on the particle velocities or surface temperatures or on the plasma jet velocity in the first two centimeters downstream the nozzle exit, we could not compare the experimental results with the two-dimensional model developed in Section 2.3.1; however, this model gives good indications about the behavior of the particles. To test the validity of the equations used and of the different coefficients (drag coefficient, Nusselt number, etc.), we consider a one-dimensional model using the same equations and calculate the velocities of the particles along the jet axis introducing as initial velocity the velocity measured on the axis as close as possible to the nozzle exit.[19] For different particle sizes the computed particle velocity along the centerline of the plasma jet is superposed on the experimental measurements in Fig. 7.

The agreement between the calculations and the measurements is relatively good for the 18-μm particles. The deviation (less than 8%) between model predictions and experimental values noted for the particle sizes could be related to the uncertainties in the plasma velocity measurements in the core region. For example, an increase of 5% of the plasma velocity gives good agreement for the 23-μm particles and a greater calculated velocity for the 18-μm particles. Just the same, it seems to indicate that the values of the drag coefficient are not too far from reality.

b. Surface Temperatures. The injection velocity is also very important for the maximum surface temperature which particles can attain, as can be seen in Fig. 10. The maximum surface temperature for 18-μm alumina particles is obtained for almost the same injection velocity as for the maximum axial velocity, and similar results hold for the different diameters considered and for the Ar–H_2 plasma.

Figure 11 shows the experimental surface temperature of 18-μm-diameter alumina particles injected with the optimum velocities in N_2–H_2 (injection velocity 25 m/s) and Ar–H_2 (injection velocity 32 m/s) plasma jets at 29 kW and 20 kW, respectively. We note that these results have been obtained for a different mixture (10 Nl/mn of argon, 50 Nl/mn of nitrogen, and 10 Nl/mn of hydrogen) than the two mixtures studied (see Section 2.2.4). The highest temperature is obtained, of course, for the greatest power and for the Ar–H_2 plasma where the velocity of the 18-μm particles is about 50 m/s (i.e., 18%) smaller than in the N_2–H_2 plasma, thus corresponding to a longer residence time with similar plasma temperatures.

The influence of the radial temperature in the plasma is also important, as can be seen in Fig. 12 which represents the variation along the radius of the jet of the experimental surface temperature of 18-μm alumina particles in a 29-kW N_2–H_2 plasma for different distances from the nozzle

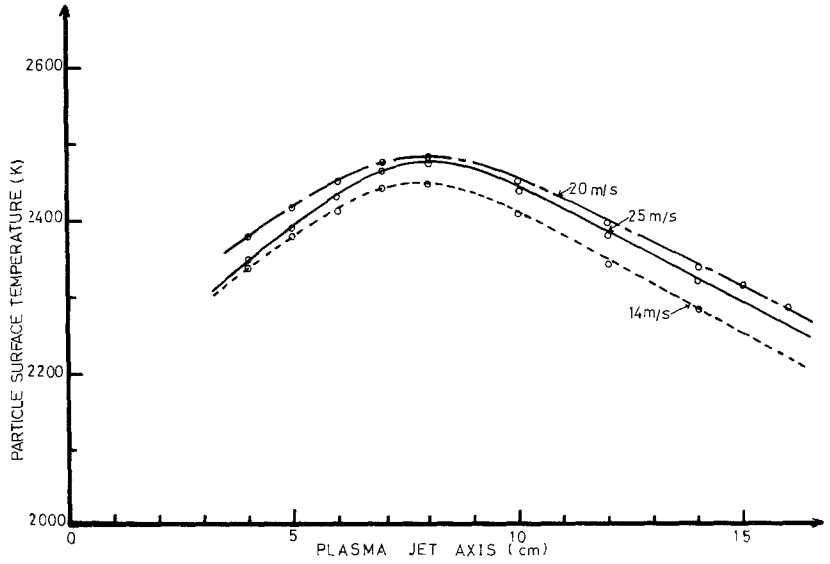

Fig. 10. Measured mean surface temperature of alumina particles (18 μm diameter) traveling along the jet axis for different injection velocities.

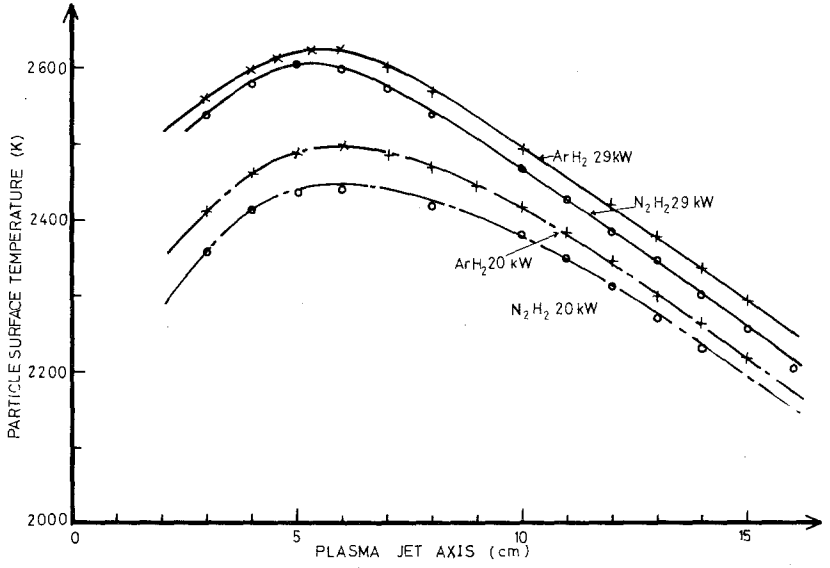

Fig. 11. Measured surface temperature of alumina particles ($d_p = 18 \pm 2$ μm) along the jet axis in N_2–H_2 and Ar–H_2 plasmas at 29 and 20 kW, respectively.

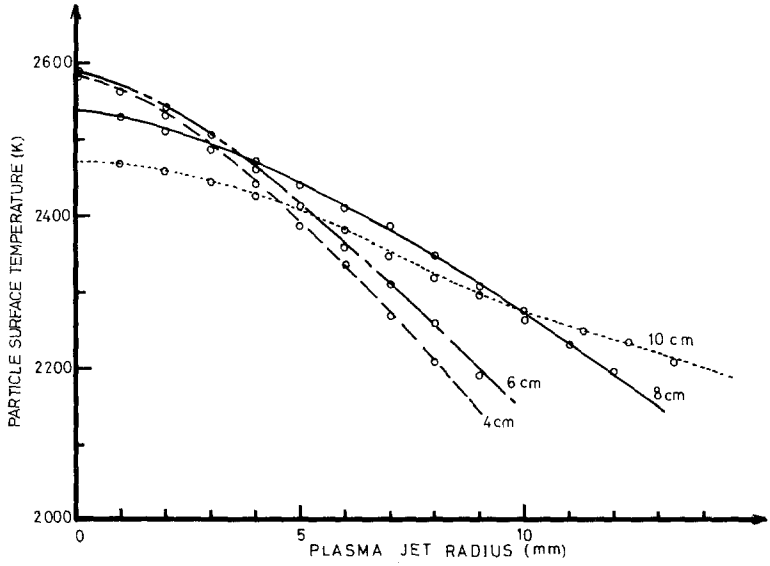

Fig. 12. Measured surface temperature of alumina particles ($d_p = 18 \pm 2$ μm) along the radius of the jet for different distances from the nozzle exit in a N_2–H_2 plasma jet of 29 kW.

exit. It is, however, important to note that the surface temperature depends little on the temperature of the plasma jet as long as this temperature is greater than 5000 K, the dissociation temperature of hydrogen, i.e., in the central part of the jet for $r < 4$ mm at 40 mm from the nozzle exit. This is due to the fact[11] that, when calculating the heat-transfer coefficient h through the Nusselt number, the conductive term is rigorously equal to 2 if the plasma thermal conductivity is taken as the mean integrated value between the plasma temperature T_p and the particle surface temperature T_s [see Eq. (1)].

Neglecting the convective term (usually between 0.3 and 0.6 for the plasma temperatures and particle diameters d considered), the quantity of heat received by the particle is then given by

$$\delta Q = \frac{2\overline{k_g}}{d}(T_p - T_s) \tag{2}$$

As with dissociation, $\overline{k_g}$ for H_2 increases by more than one order of magnitude for $T > 5000$ K and then decreases very slowly (about 6% between 5000 and 15,000 K); the heat transfer is considerably improved as soon as $T > 5000$ K and then does not vary too much when the temperature is increased from 5000 to 10,000 K.

Comparison of the calculated temperatures from a one-dimensional model, as described for the velocities[19] and where the initial temperature of the particle is measured on an axis as close as possible to the nozzle exit, shows complete disagreement between the measurements and the calculations, leading to temperatures higher than 500 K above the measured ones. This is probably due, for this one-dimensional model along the axis, to the nonequilibrium effect outside of the core of the plasma jet (ending 2 cm downstream the nozzle exit). Recent measurements have shown[37] that the kinetic temperature of the plasma (measured through rotational spectra of N_2 or N_2^+ and controlling the heat transfer) may be 2000 or 3000 K below the excitation temperature (measured through atomic line absolute intensity and used for the heat-transfer calculation of our model). As it can be seen from Fig. 2a, for a distance of 30 mm downstream the nozzle exit the excitation temperature is lower than 7000 K, corresponding to less than 5000 K of the kinetic temperature necessary for an efficient heat transfer with hydrogen.

On the other hand, the two-dimensional model indicates that the melting temperature T_m is reached during the first 6 mm of the trajectory where it has been impossible to perform velocity and temperature measurements, whereas our measurements show that the particle hardly reaches T_m at a distance 30 mm downstream the nozzle exit. Moreover, these calculations indicate that the evaporation starts after 11 mm of the trajectory, and the first results of our new two-dimensional model taking into account the evaporation indicates a reduction of about 60% of the diameter of the 18-μm particles. However, when recovering the particles in water, the mean reduction of their diameter is less than 10%. These results show clearly that our two-dimensional model is not well adapted to our measurements.

c. Fluxes. The number of particles passing at different points have been measured using a laser technique[9] (see Appendix), and the results obtained (see ref. 12) for 18-μm alumina particles in 29-kW plasmas of either N_2–H_2 or Ar–H_2 show that the majority of the particles (more than 90%) passes through the hot region of the plasma ($T > 5000$ K) where their surface temperature reaches T_m. The remaining 10% travels in the periphery of the plasma jet, does not melt at all, and has very low velocities (less than 30 m/s) compared to the mean velocities of the particles traveling in the hot zones ($v > 200$ m/s).

Using a monochromator to define a band pass of less than 1 Å at 5145 Å wavelength of the laser beam and thus reducing the plasma emission compared to the light scattered by the particles, it has been possible to determine the particle fluxes in the hot region of the plasma (from the

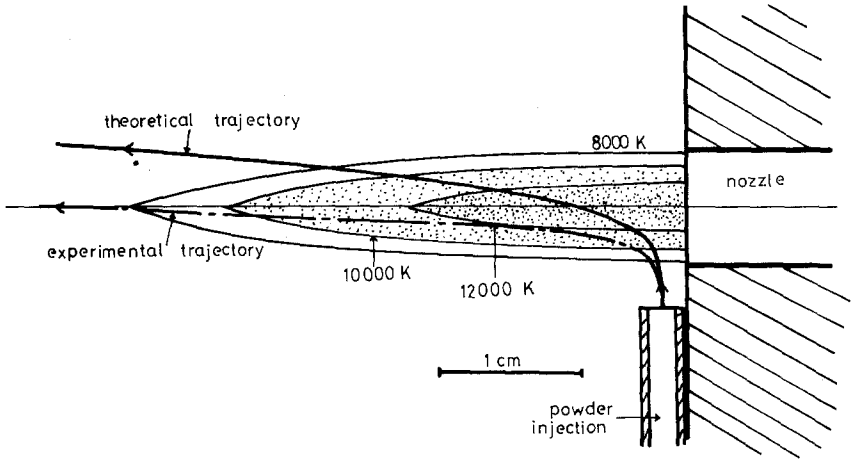

Fig. 13. Calculated and measured trajectories of 18-μm alumina particles injected at 40.5 m/s in an Ar–H_2 plasma.

nozzle exit) and thus to "see" the mean real trajectory of the particle. Such a trajectory is represented in Fig. 13. It can be seen that in spite of an injection velocity of 40.5 m/s corresponding theoretically to a particle crossing the jet axis 0.5 cm downstream of the injection exit, the real trajectory reaches the axis only after 40 mm travel, i.e., the particles travel first in the cold zones of the plasma. Such a real trajectory could explain the discrepancies between the measured and calculated temperatures. This real trajectory may be due to the neglected thermophoresis forces, the coefficients of which are certainly not accurate for gradients of 4000 K/mm (they have been measured for 200 K/mm!) and it also may be due to the striction of the plasma jet by the cold-gas injection as demonstrated by Lee *et al.*[20]

3. THE SPRAYED COATINGS

The physical properties of a coating for a given material depend largely on the spraying conditions. Although the spraying conditions depend on a large number of macroscopic parameters (see Table I), from a microscopic point of view there are only two parameters: the velocity and the bulk temperature of the particles upon impact on the substrate. Thus, in this section we will examine first the deposition of the coating as a function of these two microscopic parameters, considering especially two properties, the porosity and the crystal structure, and the correlations between these

properties for the alumina-sprayed deposits and the thermal treatment of the particles in the plasma.

3.1. Coating Generation and Physical Properties of the Coating

3.1.1. Coating Generation

In a commercial spraying process, the mean mass flow rate of the sprayed powder is about 1–2 kg/h for the 30–50-kW plasma generators used. For a spraying time of 1 h and for 30-μm-diameter particles this flow rate corresponds, taking into account the mean velocity of the relative particle-target displacement, to about 10^8 particles/m^2. During the time of freezing of a particle (10^{-7} to 10^{-6} sec[21]), about 50 to 100 particles arrive per square meter. During the freezing, and supposing that the ratio of the flattened particle to its initial diameter is about 6, a fraction of 10^{-6} to 10^{-7} of the surface is covered. The arrival of the next particle on the same spot takes about 0.1 sec, i.e., about 10^5 times the freezing time. Therefore, the process of the removal of the heat content from one particle will not be influenced by another particle. Then the coating is built up of flattened particles and consists of successive layers of materials.[2]

Heat-transfer calculations show that freezing of the particles occurs in a few microseconds and that complete cooling amounts to perhaps 100 μsec. The zone of thermal effect in the underlying material is, therefore, quite small and temperature gradients reach $\simeq 10^5$ K cm^{-1}. The coating has a sandwich-like structure as shown in Fig. 14, and its properties can be

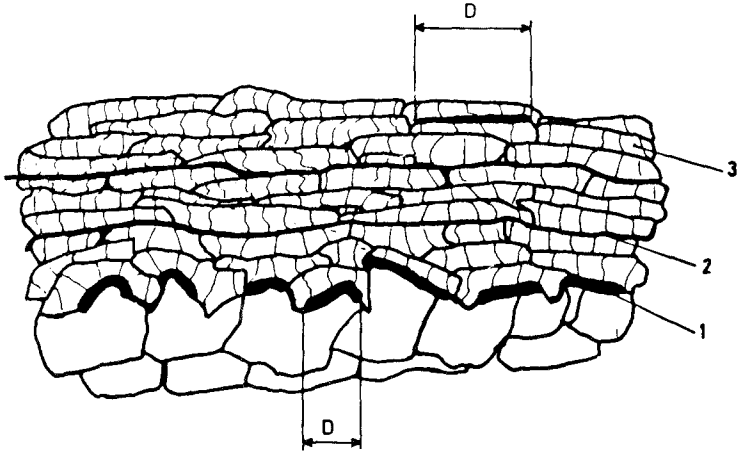

Fig. 14. Structure of plasma-sprayed coatings (from ref. 2): (1) contact with the substrate; (2) contact between solidified flattened particles; (3) cracks in the solidified particles.

regarded as resulting from the deformation and solidification processes of individual particles and/or their interaction on contact. The wetting and flow properties of the liquid droplets are of major importance since they will influence porosity within the coating and at the substrate interface.

The flow and solidification of molten particles on impact with a cold surface is a very difficult problem treated, for example, by Madejski,[22,23] and includes surface tension, viscosity, and crystallization effects. Simplifying his treatment by neglecting the surface tension (small for plasma spraying conditions) and assuming that the liquid droplet flattens before solidification occurs,[24] we obtain the degree of flattening (the ratio of the diameter D of the flattened disc to the initial particle diameter d):

$$D/d = 1.29\left(\frac{\rho v d}{\mu}\right)^{0.2}$$

where ρ is the liquid density, μ is the liquid viscosity, and v is the particle velocity upon impact.

Substitution of the appropriate values for Al_2O_3 in the velocity range 100–300 m/s yields $D/d = 3$–6, in reasonable agreement with experimental results. Evaluation of D/d for various temperatures and velocities shows that the temperature, if it is greater than the melting temperature, has a greater influence on this ratio than the velocity and that it is more important to have lower velocities and thus longer residence times, assuming $T > T_m$.

In conclusion, it may be seen that the structure of a coating will depend on the velocity, temperature, and size of the particles at the moment of impact. Analysis of the process is, however, difficult because of the statistical distribution of each of these parameters, and it is only possible to make some general theoretical predictions.[8] Such analysis is, however, of considerable importance in the interpretation of experimental studies of coating structure.

3.1.2. Crystal Structure

In plasma spraying the cooling rate of the flattened particles is very high, especially if the coating is cooled while spraying by an air blast to prevent heating by plasma gases and to remove the sensible heat and heat of fusion of the sprayed particles. Estimated heat-transfer coefficients[8,25] under these conditions are of the order of $10^5\ W\ m^{-2}\ K^{-1}$, and applying it to Al_2O_3 gives cooling rates of $10^7\ K\ sec^{-1}$ and freezing times of about 10 μsec. Such conditions may result in the suppression of crystallization or in the formation of metastable phases, as observed under similar conditions in splat quenching. The classic example of this effect is provided by

alumina coatings which consist predominantly of one or more of the many metastable phases (eta, gamma, delta, theta) rather than α-Al_2O_3, the only stable structure.[26] The formation of metastable phases may be explained on the basis of a lower free energy for nucleation of the spinel type structure from the liquid when it is undercooled well below the equilibrium melting point as a result of rapid cooling.[27] The phase finally observed depends on the rate of transformation from one metastable form to another and to α-Al_2O_3, and on the cooling rate of the solid after solidification. This explains the observations that different metastable phases are observed depending on the spraying conditions, size and shape of particles, and the temperature of the substrate.[28] It is necessary to heat the substrate to more than 1100°C to obtain a coating consisting completely of α-Al_2O_3[29] and to 1450°C to obtain a well-sintered deposit.[30] The α-Al_2O_3 present in conventional coatings (10–25%) is probably due to incomplete melting of the powder feed, resulting in the presence of α-Al_2O_3 in the droplets on impact[26] which acts as nuclei for crystallization. Although a deposit of metastable alumina may be heat treated to transform it to the more desirable α-Al_2O_3 form, for the preparation of bodies for spraying onto a removable core, the relatively large change in the true density, from 3.6 for γ-Al_2O_3 to 4.0 for α-Al_2O_3, results in an increase in porosity and consequently a degradation in mechanical properties.[31]

3.1.3. Porosity

The nature of coating formation by impact and solidification of separate droplets necessarily results in some porosity which generally lies in the range 5–20% and depends both on spraying conditions and on the material being sprayed. All the particles have the same mean direction when arriving at the substrate[1] (we have seen in Fig. 9 that the radial component of the velocity is low, corresponding to an angle of divergence from the axial trajectory of less than 2°). Consequently a shadow effect occurs, causing porosity. The liquefied and ductile particles have the opportunity to accommodate somewhat to the irregularities of the surface, but not completely. Narrow holes cannot be filled out. The atoms lack the mobility of a fluid because of the very high freezing rates. The valleys in the surface of a substrate or the lamellae can include some air or gas, causing pores or adherence failures. The particle may burst during the flattening process to a lamella. A material-dependent effect may be seen from a classification given by Metco.[32] For example, TiO_2, Al_2O_3–50% TiO_2, Cr_2O_3, and NiO are included in a group in which porosities of less than 4% may be achieved; spinel, mullite, Al_2O_3, and ZrO_2 are in a group of 4–8%, and rare earth oxides and zircon fall in a group of 8–15%.

This variation with composition is perhaps associated with the wetting characteristics of the various materials and related to surface tension and contact angle. It is interesting to note that the surface tension of TiO_2 is about half that of Al_2O_3 at their respective melting points[33] and that the presence of a small amount of TiO_2 ($\simeq 2.5\%$) reduces the porosity of Al_2O_3 coatings. In general, the materials giving low porosities also give the best adhesion to the substrate, which would also be expected to arise from improved wetting.

For a given coating material, the porosity is related to the particle size distribution of the powder and to the temperature and velocity of the particles on impact. Clearly the lowest-porosity coatings would be expected for a stream of completely molten particles with high velocity.

The temperature, velocity, and thermal conductivity of the gas in a plasma jet vary considerably from point to point, and, since the trajectories of individual injected particles will differ, the spray stream produced will contain particles with a wide range of velocities and temperatures. In practice, a small proportion may not be melted or be only partially melted[7,34] or have low velocities, and these will tend to reduce the quality of the coating. This effect can be reduced to some extent by a compressed air blast normal to the plasma jet and close to the substrate, which removes a large proportion of the particles which have not mixed properly with the plasma and thus have low velocities.[35]

3.2. Influence of Spraying Conditions on the Properties of the Alumina Coatings

The open porosity P_o of the plasma-sprayed coatings has been measured using a mercury porosimeter, and we have studied the structure of the porosity by scanning electron microscopy of transverse fracture surfaces of detached deposits. This last technique reveals isolated, approximately spherical pores within the lamellae, sometimes connected by very fine cracks, and flat pores arising from incomplete adhesion between lamellae.[8,12]

The ratio $R = \alpha/(\alpha + \gamma)$ has been measured by X-ray analysis by comparing the intensity of different lines to the ones given by calibrated mixtures of α and γ (α being the volumetric quantity of alumina in the stable α-phase in the deposit and γ the quantity of alumina in the metastable γ-phase).[7]

3.2.1. Spraying Geometry

As we have demonstrated in the preceding section, to obtain dense coatings the particles must impinge on the substrate in the liquid state with

the greatest kinetic energy and the lowest viscosity in the liquid state in order to have the best flattening on the substrate and to accommodate somewhat the irregularities of the surface. Of course these requirements are incompatible: a high velocity reduces the residence time and thus the temperature of the particle, and since the highest temperature (the whole particle has to be melted) is the most important parameter (lowest particle viscosity), the target must be located a few millimeters downstream of the point where the particles reach the maximum surface temperature (in order to have the temperature of the center as high as possible; cf. Section 2.3.1) even if this location does not correspond to the maximum of velocity. Figure 15 shows, for alumina particles ($18 \pm 2\ \mu m$) in a N_2–H_2 plasma at 20 kW, the axial velocity and surface temperature as a function of the distance from the nozzle exit. The best location of the target is downstream of the maximum temperature: this location corresponds to a porosity P_o of 9% and a ratio $R = \alpha/(\alpha + \gamma)$ of 6%; a location 10 mm upstream gives $P_o = 12\%$ and $R = 9\%$; and a location 10 mm downstream gives $P_o = 13\%$ and $R = 10\%$!

Another very important parameter is elimination of the particles that did not penetrate into the hot zones of the plasma and that travel at the

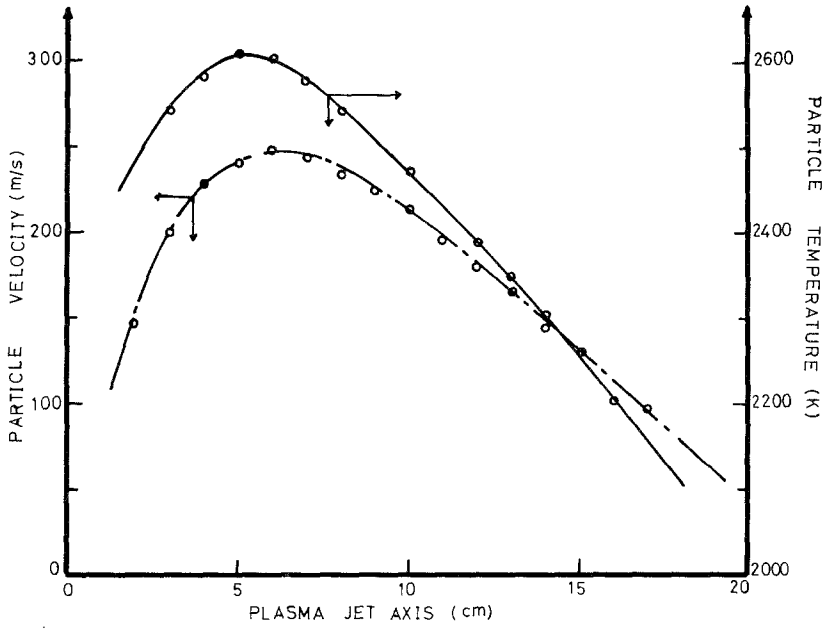

Fig. 15. Experimental axial mean velocity and surface temperature of 18-μm Al_2O_3 particles as a function of the distance from the torch exit (N_2–H_2 plasma at 29 kW).

periphery of the jet with a low velocity (less than 30 m/s) and low temperature (less than 1000 K) and thus form solid inclusions in the coating and reduce its mechanical properties. This effect can be reduced to some extent by a compressed air jet blast normal to the plasma jet[35] which removes a large proportion of the particles having low velocities and traveling in the periphery of the jet. The position of this barrier and the air flow rate is very important[35] because the velocity and surface temperature of the particles are reduced behind it. Thus the best position is one as close as possible to the substrate, and the air flow rate has to be adjusted to a value corresponding to the maximum elimination of low-velocity particles and to the smallest reduction of their surface temperature. All the results presented below have been obtained under these conditions, the substrate being at 60 mm from the nozzle exit and the air barrier disposed 15 mm upstream. This can be seen in Fig. 16 which shows, just

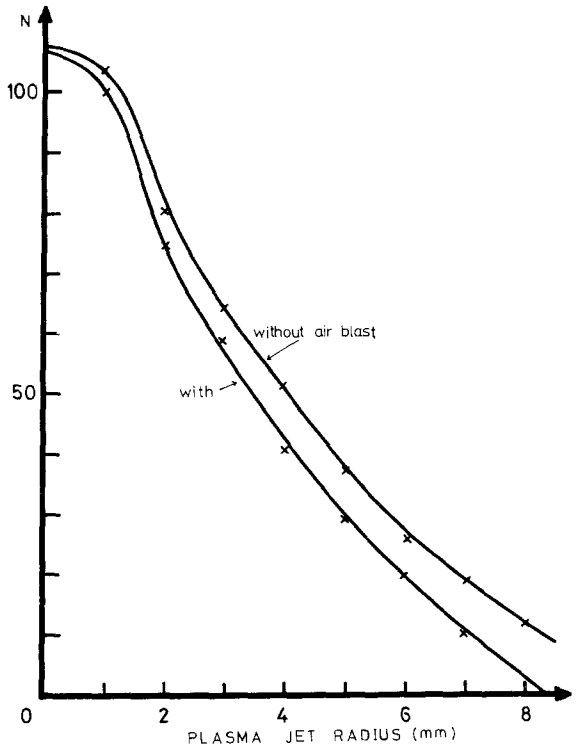

Fig. 16. Influence of an air-barrier blast normal to the plasma jet on the radial flux of the particles (just behind the barrier). N is the number of particles crossing a section of 2.3×10^{-2} mm^2 in 1 s (N_2–H_2 plasma at 29 kW).

behind the air jet, the number of particles crossing a section 2.3×10^{-2} mm^2 in 1 sec as a function of the plasma radius (the method used to measure the particle number is described in the Appendix). The air blast eliminates 15% of the total number of particles: 5% of those having a radial coordinate of less than 4 mm and 10% of the other particles; it also eliminates all the particles having a radial coordinate greater than 8 mm.

If one now considers the axial velocity and surface temperature of the particle, it can be seen that:

the air pressure creates a radial component of the velocity of the particles, thus reducing the maximum axial velocity (from 275 to 270 m/s) and reducing even more the velocity after the air barrier (see Fig. 17),

the surface temperature of the particles is lowered while crossing the air flow (crossing time about 20 μs); this is due, first, to the crossing of the air flow and, second, to the fact that the air flow cools considerably the plume of the plasma behind it (see Fig. 18).

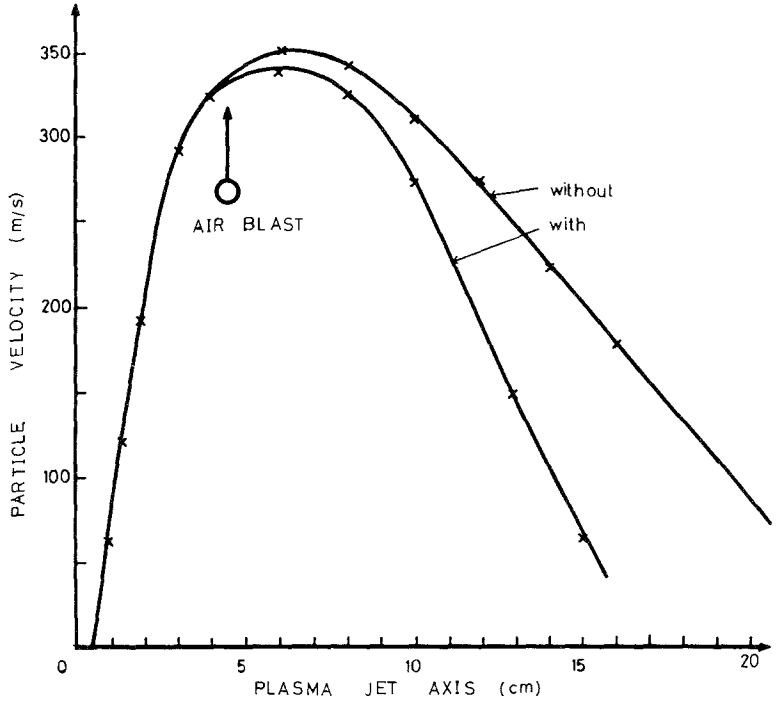

Fig. 17. Influence of an air-barrier blast normal to the plasma jet on the experimental velocity of 18-μm-diameter alumina particles (N_2–H_2 plasma at 29 kW).

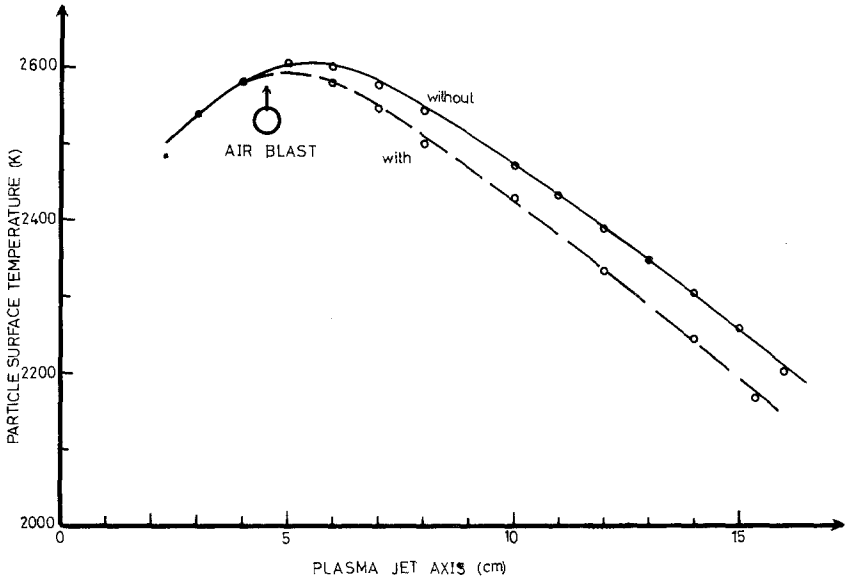

Fig. 18. Influence of an air-barrier blast on the measured surface temperature of alumina particles of 18 μm diameter traveling along the jet axis (N_2–H_2 plasma at 29 kW).

3.2.2. Nature of the Plasma Gases

The major difference between the two gas mixtures used was the higher velocities achieved for N_2–H_2 at the same power input (Fig. 19), a result which can be rationalized on the basis of differences in the properties (viscosity, thermal conductivity) of the gases at high temperature.[13]

Thus the traveling time through the hottest regions of the Ar–H_2 plasma is longer (about 20% longer), and the particles reach a higher temperature (Fig. 12). The loss in kinetic energy is overcompensated by the increase in temperature, and the droplets spread better. The porosity of the deposits is lower: 3% instead of 9%. In addition, the tip of the flame is longer and the plume more expanded, which leads to a more uniform treatment of the powders. The fraction of particles treated under optimum conditions is greater and the α-content of the deposit lower: 1% instead of 6%.

3.2.3. Electrical Power Input to the Torch

The measured axial mean velocity for 18-μm particles as a function of distance from the plasma torch exit is shown in Fig. 19 for the N_2–H_2

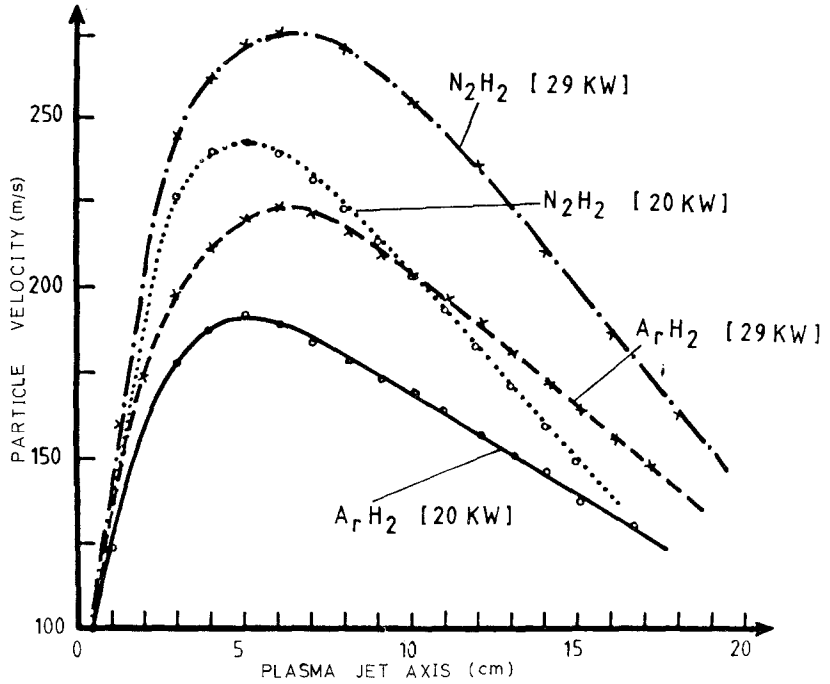

Fig. 19. Experimental axial mean particle velocity as a function of distance from the torch nozzle exit for both gas mixtures at 20 and 29 kW.

and Ar–H_2 plasmas at 20 and 29 kW input. As expected, the particle velocity increases with power input. The distance of the peak velocity region increases from ≈50 to ≈70 mm from the torch exit as the power input was changed from 20 to 29 kW for both gas mixtures.

The experimental mean surface particle temperature as a function of distance from the torch exit is shown in Fig. 11 for both gas mixtures at 20 and 29 kW. This shows that the mean particle surface temperature reaches the melting point of Al_2O_3 at 20 kW input for both gas mixtures but reaches higher temperatures over a short distance (40–70 mm from torch exit) at 29 kW. Thus, increasing the power input for a given gas mixture, increases the peak considerably but results in little change in temperature because the residence time in the hot zone is approximately the same. Thus, the effect of increasing power input is to increase the number of particles which are completely molten with little change in the mean temperature; this appears to be the case at 29 kW input. Except for

N_2–H_2 plasma at 20 kW, the α-phase fraction in the deposits remains rather constant and lower than 2% for other optimal working conditions. This α-residual content appears difficult to reduce considering the kinetics of the γ–α transformation.[36]

The porosity decreases with increasing power input for both gases, but lower porosities are achieved with Ar–H_2 than N_2–H_2 (see Table III).

CONCLUSION

In D.C. plasma jets, measurements of the velocity and temperature distributions both of the plasma jet and of the solid particles injected into them are very useful in understanding what thermal treatment the particles undergo during their flight in the plasma and thus to deduce the relationship between spraying operating conditions and the properties of the coating.

Using spraying devices with operating conditions similar to those used in industry, we have developed the measurements of the plasma jet and of the particles in flight by emission spectroscopy, laser Doppler anemometry, and statistical pyrometry in flight. It is thus possible, for alumina particles of given diameters (narrow size distributions), to correlate the velocity and surface temperature of the particles at the moment of their impact on the substrate with the macroscopic parameters for spraying (arc parameters, gas nature and flow rate, etc.).

With such measurements it is thus possible to optimize the spraying conditions to obtain, for example, dense coatings of alumina (porosity of less than 2%) essentially in the γ-form (more than 99%).

In order to better understand what happens during the thermal treatment of the particles, a two-dimensional model has been developed including heat and phase-change propagation but neglecting thermophoresis forces and evaporation. For this model the temperature and velocity distributions within the plasma jet (assumed to be unperturbed by the particles and carrier gas injection) and the injection velocity of the particles are used as the initial values.

Unfortunately a straightforward comparison of the calculations of the model with our experimental results cannot be made due to the impossibility of measuring the particle velocity and surface temperature in the first two centimeters downstream the nozzle exit (where the plasma luminosity is too high compared to the light emitted or scattered by the particles).

Thus, in order to verify the validity of our equations and the calculated values for the drag coefficient and the heat-transfer coefficient, we have developed a one-dimensional model where we have introduced as initial values the velocity and surface temperature of the particles along the jet axis measured as close as possible to the nozzle exit. Along the jet axis

Table III. Relationship between Porosity and Power Input

Power input	N_2–H_2			Ar–H_2		
	Porosity (%)	Mean pore size (μm)	Percent α-Al_2O_3	Porosity (%)	Mean pore size (μm)	Percent α-Al_2O_3
20 kW	11	0.15	5.5	5.5	0.11	2
29 kW	9	0.11	4	2	0.09	1.5

the calculated and measured velocities are equivalent to within 5% (along this axis and 2 cm downstream the nozzle exit the temperature gradients are less than 100 K/mm and the thermophoresis forces are negligible). However, the discrepancies between the calculated and measured surface temperatures are important (more than 500 K when taking into account the heat propagation into the alumina particles and more than 1000 K with no heat propagation). This might be due to the fact that the heat-transfer coefficient is overestimated or more probably that the measured excitation temperature (absolute line intensity) is also overestimated compared to the kinetic temperature which governs the transport phenomena. Very recent measurement[37] performed using rotational spectra have shown that the rotational temperature (equal to the kinetic temperature) may be 2000 or 3000 K smaller than the excitation temperature outside the core of the plasma jet (2 cm downstream the nozzle exit), thus reducing the heat transfer along the axis in the one-dimensional model.

The two-dimensional model predicts that the surface temperature of the particles should reach the melting temperature T_m at a distance 10 mm downstream the nozzle exit, but our measurement shows that T_m is reached only after 30 mm or more where the two-dimensional model indicates that the particles start to vaporize. As the excitation temperature of the plasma is equal to the rotational temperature in the core of the plasma jet,[10,37] another explanation has to be found. In this case, the differences may be attributed to the influence of the carrier gas perturbing the plasma and also to the thermophoretic forces, the most recent measurements showing that the particles do not really penetrate into the hot zones of the plasma even if their injection velocity is twice the optimal calculated one.

To develop a more realistic model, the following conditions have to be met:

Improvement of the measurements is necessary (measurement of the rotational temperature, of the influence of the carrier gas, and of the particle velocity and surface temperature in the core of the plasma jet).
The thermophoretic forces (due to the high radial temperature gradients: up to 4000 K/mm, in the injection area) have to be taken into account with the measured thermophoretic coefficients to determine the real particle trajectories.
The surface vaporization with the propagation of a vaporization front has to be included into the model.

With such calculations it would be possible to optimize the spraying conditions taking into account the nozzle dimensions, the nature of the gas and the gas flow rate, the nature and diameter of the particles, etc.

APPENDIX

Description of the Experimental Methods used

In the plasma jet core, the spatial distribution of *the plasma jet temperature* is deduced from measurement of the volumetric emission coefficient ε of atomic lines. Local thermodynamic equilibrium L.T.E. is assumed (the electron density is greater than 10^{16} cm^{-3} in the core of the plasma jet). The plasma composition is calculated at atmospheric pressure as a function of temperature, and the temperature is deduced from the measured value of ε.[10] The experimental setup used for the spectroscopic measurements consisted essentially of a J.Y. THR 1500 monochromator equipped with a holographic grating with 3200 lines/mm and a dispersion of 1.1 Å/mm. The system is calibrated using a standard tungsten ribbon lamp. Step-to-step motors control the displacement of the plasma jet (two axes in a vertical plan) and of the grating. This method is thus well suited for automation of the measurements (computer controlled) taking into account Abel's inversion, despite the requirements of L.T.E. and absolute energy calibration. The precision of the measurement is within 5%.

The *particle surface temperature* is determined by in-flight pyrometry[8]: an image of the plasma jet is focused onto the entrance slit of a cooled photomultiplier (RCA C31 034C) sensitive in the near infrared over the spectral range 850–1050 nm. The amplitude of current pulses generated by the passage of each particle across the measuring volume is a function of the particle diameter, its shape, surface emissivity, and temperature. The signals are amplified, shaped, and analyzed by a multichannel analyzer. A calibration simulating particle of known temperature and emissivity is needed. This was carried out using a tungsten ribbon lamp placed behind a chopper having a small aperture and rotating at a constant speed.

The precision error is estimated to be about 5%. However, uncertainties in the values of the surface emissivities of the sprayed material could introduce an accuracy error of about 15% in the temperature.

The *particle velocity distribution* within the plasma jet is measured by a Doppler laser velocimetry technique with interferential setup.[8] In the later technique a 1.2-W argon ion laser beam ($\lambda = 514.5$ nm) is split into two beams which are focused to form an interference fringe pattern in the flow region. As a particle passes through the fringes, it produces a light burst modulated at a frequency which is a function of its velocity component orthogonal to the fringes and of the fringe spacing. The scattered light is collected by a lens and concentrated on the entrance slit of a photomultiplier; the electrical signal delivered by the photomultiplier is processed by a photon-correlation method. Observations of the light scattered by the particles are made at 90° to the laser axis in order to improve spatial

resolution: the measuring volume is limited to a cylinder of 600 μm diameter and 1.1 mm length; the fringe spacing is 100 μm.

The axial and radial velocity components of the velocity could be obtained by rotating the fringe pattern around its axis.

The precision of the fringe spacing measurement is about 1%, and the velocity measurement precision is estimated to be 5%. To measure the plasma velocity more precisely—the velocity of fine alumina tracer particles (3 ± 1.5 μm) dispersed in the flow—the two-point measurement system is used. In this system, the laser beam passes through a beam splitter and a microscopic lens which forms two coherent beams which are focused down to two spots in the plasma jet by a lens with a magnification of 1. As a particle crosses each of the focus volumes, it scatters a light pulse and the particle velocity is deduced from the time between two successive pulses. Each beam focus is imaged onto the entrance slit of two photomultipliers equipped with a narrow band filter. The output of the two photomultipliers is cross correlated by the photon correlator. The sampling volume is a cylinder with 600 μm diameter and 100 μm length.

The particle flux in the plasma jet is measured by counting, during a given time, the pulses resulting from the light scattered by the particles passing through a focused laser beam.[8]

REFERENCES

1. J. H. Zaat, *Proceedings of the 9th International Thermal Spraying Conference*, La Haye, May 23–29, 1980.
2. N. N. Rykalin and V. V. Kudinov, *Pure Appl. Chem.* **48**, 229 (1976).
3. J. L. Besson, M. Vardelle, and P. Boch, *Ind. Ceram.* **727**, 248 (1979).
4. A. Vardelle, P. Fauchais, and M. Vardelle, Projection de revêtements protecteurs par plasma, Actual. *Chim.* **10**, 69 (1981).
5. R. M. Gage, Arc torches and process, U.S. Patent No. 2, 806, 124 (1957).
6. E. Pfender, Electric arcs and gas heaters, in *Gasesous Electronics*, Vol. 1, M. N. Hirsch and H. J. Oskam, eds., Academic Press, New York (1978), p. 291.
7. F. Kassabji and P. Fauchais, *Rev. Phys. Appl.* **16**, 549 (1981).
8. M. Vardelle, Etude de la structure des dépôts d'alumine obtenus par projection plasma en fonction des températures et des vitesses des particules au moment de leur impact sur la cible, Thèse de 3ème cycle, Université de Limoges, March 26 (1980).
9. A. Vardelle, J. M. Baronnet, M. Vardelle, and P. Fauchais, *IEEE Trans. Plasma Sci.* **8**, 417 (1980).
10. J. M. Baronnet, Contribution à l'étude spectroscopique des plasmas d'azote produits par un générateur à arc soufflé; application à la chimie des plasmas: synthèse des oxydes d'azote, Thèse d'Etat, Université de Limoges, November (1978).
11. E. Bourdin, P. Fauchais, and M. Boulos, Transient heat conduction under plasma conditions, *Int. J. Heat Mass Transf.* (1982), accepted for publication.
12. M. Vardelle, A. Vardelle, J. L. Besson, and P. Fauchais, *Rev. Phys. Appl.* **16**, 425 (1981).
13. C. Gorse, Contribution au calcul des propriétés de transport des plasmas des mélanges

argon-hydrogène et argon-azote, Thèse de 3ème cycle, Université de Limoges, September 9 (1975).
14. E. Bourdin, Contribution à l'étude théorique et expérimentale des nitrures et d'oxynitrures par réactions de jets de plasma d'azote avec des poudres d'aluminium et de silicium et leurs oxydes, Thèse de 3ème cycle, Université de Limoges, March 16 (1976).
15. M. Boulos, *IEEE Trans. Plasma Sci. PS*-6, 93 (1978).
16. T. Yoshida and K. Akashi, *J. Appl. Phys.* **48**, 2252 (1977).
17. W. D. Murray and F. Landis, *Heat Transf.* **81**, 106 (1959).
18. P. Jamet and R. Bonnerot, *Int. J. Numer. Methods Eng.* **8**, 811 (1974).
19. M. Vardelle, A. Vardelle, P. Fauchais, and M. I. Boulos, Plasma-particle momentum and heat transfer: modelling and measurements, *AIChE J.* (1982), accepted for publication.
20. Y. C. Lee, K. C. Hsu, and E. Pfender, Modelling of particles injected into a D.C. plasma jet, in *Proceedings of the 5th International Symposium on Plasma Chemistry*, Heriot Watt University, Edinburgh, August 10–14, 1981, p.795.
21. J. J. Houben, Remarks concerning a rational plasma for thermal spraying, *Proceedings of the 9th International Thermal Spraying Conference*, La Haye, May 19–23, 1980, p. 143.
22. J. Madejski, *Int. J. Heat Mass Transf.* **19**, 1003 (1976).
23. J. Madejski, *Bull. Acad. Pol. Sci.* **24**, No. 1 (1976).
24. P. Fauchais, E. Bourdin, J. F. Coudert, and R. McPherson, High pressure plasmas and their application to ceramic technology, in *Plasma Chemistry*, Vol. 3, M. Venugopalan and S. Veprek, eds., Springer-Verlag, Berlin (1982), to be published.
25. H. Jones, *Rep. Prog. Phys.* **36**, 1425 (1973).
26. P. Zoltowski, *Rev. Int. Htes Temp. Refract.* **6**, 65 (1968).
27. R. McPherson, *J. Mater. Sci.* **8**, 851 (1973).
28. T. W. Sokolova, I. R. Kozlova, Kh. Derko, and A. V. Kiiko, *Izv. Akad. Nauk SSSR Neorg. Mater.* **9**, 611 (1973).
29. F. Eichorn, J. Metzler, and W. Eysel, *Metallorberflaeche* **26**, 212 (1972).
30. J. B. Kaffachine and A. G. Thomas, *Powder Met.* **7**, 290 (1964).
31. V. S. Thompson and O. J. Whittemdre, *Ceram. Bull.* **47**, 637 (1968).
32. H. S. Ingham and A. D. Shepard, *Mecto Flame Spraying Handbook* (1965).
33. B. S. Mitin and Yu. A. Nagibin, *Izv. Akad. Nauk SSSR, Neorg. Mater.* **7**, 814 (1971).
34. S. K. Kitahara and A. Hasni, *J. Vac. Sci. Technol.* **4**, 142 (1974).
35. J. Guyonnet, Brevet C.N.R.S. 124111 et additifs 168044 et 7044678.
36. R. McPherson, *J. Mater. Sci.* **15**, 3141 (1980).
37. J. F. Coudert, J. M. Baronnet, A. Catherinot, and P. Fauchais, Time-resolved measurements of rotational temperature in a N_2/O_2 D.C. plasma jet, *Seventh International Conference on Gas Discharges and Their Applications*. London, August 31 to September 3, 1982.